Research Square

Preprints are preliminary reports that have not undergone peer review.
They should not be considered conclusive, used to inform clinical practice,
or referenced by the media as validated information.

Numerical Assessment of Sedov and RMV Blast Waves with an Eulerian Hydrodynamics Solver

Jie-Dong Cao
Institute of Applied Physics and Computational Mathematics
Meng-Juan Xiao
xiao_mengjuan@163.com
Institute of Applied Physics and Computational Mathematics
Hui-Po Liu
Institute of Applied Physics and Computational Mathematics
You-sheng Zhang
Institute of Applied Physics and Computational Mathematics

Research Article

Keywords: blast wave, Sedov problem, RMV problem, nonlinear heat conduction, numerical reliability

Posted Date: November 24th, 2026

DOI: https://doi.org/10.21203/rs.3.rs-11186078/v1

License: This work is licensed under a Creative Commons Attribution 4.0 International License.
Read Full License

Additional Declarations: No competing interests reported.

Numerical Assessment of Sedov and RMV Blast Waves with an Eulerian Hydrodynamics Solver

Jie-Dong Cao[1], Meng-Juan Xiao[1,2*], Hui-Po Liu[1,2], You-sheng Zhang[1,2,3]

[1]Institute of Applied Physics and Computational Mathematics, Beijing, 100094, China.
[2]National Key Laboratory of Computational Physics, Beijing, 100088, China.
[3]Center for Applied Physics and Technology, HEDPS, and College of Engineering, Peking University, Beijing, 100871, China.

*Corresponding author(s): Meng-Juan Xiao. E-mail(s): xiao_mengjuan@163.com;

Abstract

The numerical behavior of strong blast waves is assessed for the classical Sedov problem and the nonlinear-heat-conduction RMV (Reinicke Meyer-ter-Vehn) problem. Sedov plane-, line-, and point-blast calculations and an RMV point-blast calculation are compared with reference solutions from ExactPack through field contours, radial profiles, error norms, and grid-refinement studies. The computed wave fronts and profiles approach the reference solutions as the grid is refined, while the point-blast velocity retains the largest error and near-origin oscillations among the Sedov geometries. Angular profiles show that density and pressure symmetry is well preserved for the refined Sedov point blast and that the directional variation of the RMV thermal wave decreases on the finest grid. The source-region study identifies a distinct initialization effect: enlarging the deposition region displaces the shock, and grid refinement at fixed physical source size improves peak resolution without removing this wave-front bias. In the RMV benchmark, density, velocity, and temperature exhibit approximately first-order measured convergence and weaker central velocity oscillations than in the classical Sedov point blast. These results isolate central discretization, source regularization, and heat-conduction-coupled behavior as separate reliability considerations in multidimensional blast-wave calculations.

Keywords: blast wave, Sedov problem, RMV problem, nonlinear heat conduction, numerical reliability

1 Introduction

The Sedov blast-wave problem is a classical test in computational hydrodynamics, describing the self-similar expansion of a strong shock from a localized energy source into a uniform medium. Its similarity solution[1, 2] provides a benchmark for assessing shock propagation, symmetry preservation, and energy redistribution. Detailed evaluations of Sedov reference solutions and their numerical use have been reported by Kamm[3, 4] and Pederson et al.[5], while code-verification metrics for comparing numerical and reference solutions have been discussed by Kamm et al.[6]. The problem has also served as a canonical model for blast-wave dynamics in astrophysics[7, 8] and laser-driven or inertial-confinement-fusion research[9–11].

For compressible-flow calculations, the numerical treatment of strong discontinuities depends on the reconstruction, limiting, and Riemann-solver choices. High-resolution finite-difference

and finite-volume methods developed from Godunov-type formulations[12–14] remain widely used, with weighted essentially non-oscillatory (WENO) reconstructions providing robust accuracy near shocks[15]. HLLC-type approximate Riemann solvers restore the contact wave in the original HLL framework[16], while multidimensional limiting and reconstruction strategies have been developed for compressible flows[17, 18]. Numerical dissipation, entropy generation, and low-Mach behavior of high-resolution shock-capturing schemes have also been examined in detail[19–21]. These methodological studies motivate using Sedov configurations to separate errors associated with shock capturing, geometric source terms, and initialization from errors associated with the underlying physical model.

However, many applications involve coupled hydrodynamics and thermal transport. In high-temperature plasmas, heat conduction can significantly alter blast-wave dynamics and the structure of compressible flows. This issue is relevant to high-energy-density and inertial-fusion applications, where hydrodynamic instabilities, thermal transport, and drive asymmetry interact[22–26]. To extend the verification framework to such regimes, the point explosion with heat conduction–often referred to as the RMV (Reinicke Meyer-ter-Vehn) test problem–has been developed[27]. This problem considers a strong point explosion in a cold gas with nonlinear heat conduction, yielding two spherical waves–a shock wave and a thermal wave. Their fronts generally propagate at different speeds, and their relative ordering depends on the parameters and time. Self-similar solutions exist when the ambient gas density decays with a prescribed power of the radius. If the initial explosion energy is small, the diffusive effect is limited to a region behind the shock. If the explosion energy is sufficiently large, the thermal front precedes the hydrodynamic front, which is then an isothermal shock. Shestakov[28] and Ghosh et al.[29] studied point explosions with heat conduction using a coupled hydrodynamic diffusion code and a fully implicit radiation-hydrodynamics code, respectively. These studies provide historical context for heat-conduction-coupled blast-wave calculations. The Ghosh et al. results are used below only for a contextual comparison with a related heat-transport calculation: that study solves a radiation-hydrodynamics model, whereas the RMV model considered here contains nonlinear heat conduction without radiation transport or a radiation-energy equation. Despite its importance as a simplified test case for high-energy-density physics problems, the RMV heat-conduction problem has rarely been studied in a systematic verification context.

The objective of this study is to assess the numerical reliability of multidimensional blast-wave calculations for the pure-hydrodynamic Sedov problem and the nonlinear-heat-conduction RMV problem. The calculations are performed with CFD^2 (Code of Finite Difference for Compressible Fluid Dynamics), an Eulerian hydrodynamics code developed by Yousheng Zhang et al. since 2016. The code has been used to investigate buoyancy-, shock-, and shear-driven mixing flows in a wide range of physical conditions [30, 31] and has been assessed through simulations of classical flow cases and complex mixing flows[32–38]. The Sedov point-, line-, and plane-blast cases and the RMV point-blast case are computed in two-dimensional (2D) coordinate systems and compared with reference solutions obtained from ExactPack[1, 27]. In addition to profile errors and grid-convergence rates, the assessment separates three reliability issues that are often combined in a single grid study: the central discretization error associated with a localized point source, the persistent wave-front bias introduced by regularizing that source over a finite region, and the change in convergence and near-origin behavior in the heat-conduction-coupled RMV calculation. Angular extraction studies are used to test whether the nominally radial wave structure remains independent of direction on Cartesian and axisymmetric grids. The resulting evidence provides specific findings about the numerical representation of strong blast waves rather than only a pass–fail verification of a particular code.

This paper is structured as follows. The Sedov and RMV problem definitions are given in Section 2. The numerical models and implementations are described in Section 3. The results and discussions are given in Section 4; the conclusions are summarized in Section 5.

2 Sedov and RMV benchmark problems

2.1 Classic Sedov problems

The classic Sedov problem considers point, line, or plane explosions in an inviscid, non-heat-conducting, compressible ideal gas. These correspond to spherically symmetric, cylindrically symmetric, and plane symmetric flows, termed point-blast, line-blast, and plane-blast problems, respectively. Because the solution is self-similar, the Sedov problem is frequently used to assess shock propagation, symmetry preservation, and energy redistribution in numerical codes.

The reference solution used in this study is obtained directly from the open-source LANL ExactPack library: `https://github.com/lanl/exactpack`. Details of the reference-solution algorithm are outside the scope of this paper. Unless stated otherwise, the Sedov cases use the cgs quantities specified below: density in $\mathrm{g\,cm^{-3}}$, pressure in $\mathrm{dyn\,cm^{-2}}$, energy in erg, and time in s. The numerical values are used consistently in the initial conditions and in the reference-solution comparisons; no additional nondimensional scaling is introduced in this section. The classic Sedov problem models a rapid point-source explosion in an inviscid, non-heat-conducting polytropic gas, caused by a release of energy E_{T0} at the origin $r = 0$ at time $t = 0$. The independent fluid variables are (i) the mass density $\rho(r,t)$, (ii) the velocity of the gas $u(r,t)$, and (iii) the pressure $P(r,t)$, each at spatial location r and time t. The specific internal energy $e(r,t)$ is related to the other fluid variables by the equation of state (EOS) for an ideal gas at constant entropy, $P = (\gamma-1)\rho e$, where $\gamma \equiv c_p/c_v$ is the ratio of specific heats at constant pressure and volume. The Euler equations take the form

$$\begin{array}{l} \frac{\partial \rho}{\partial t} + u\frac{\partial \rho}{\partial r} + \frac{\rho}{r^{k-1}}\frac{\partial}{\partial r}(ur^{k-1}) = 0 \\ \frac{\partial u}{\partial t} + u\frac{\partial u}{\partial r} + \frac{1}{\rho}\frac{\partial P}{\partial r} = 0 \\ \frac{\partial}{\partial t}(P\rho^{-\gamma}) + u\frac{\partial}{\partial r}(P\rho^{-\gamma}) = 0 \end{array} \qquad (1)$$

where $k = 1, 2, 3$ for planar, cylindrical, and spherical coordinates respectively. The initial density $\rho(r,0) = 1\,\mathrm{g\,cm^{-3}}$ is taken to be constant in r, and the initial velocity and pressure $u(r,0) = 0$ and $P(r,0) = 0$ everywhere in space (for $r \neq 0$). At $t = 0^+$, an infinitely strong shock wave forms at the origin, moving radially outward, with energy E_{T0}:

$$E_0 = \int dV \left[\frac{1}{2}\,\rho u^2 + \frac{P}{\gamma - 1}\right] \qquad (2)$$

where the integration runs over the volume behind the shock at time t, i.e., the integration runs over $0 \le r \le r_{\mathrm{shock}}(t)$. The volume element takes the form $dV = 4\pi\, r^2 dr$ for $k = 3$ (spherical), $dV = 2\pi\, r dr$ for $k = 2$ (cylindrical), and $dV = dr$ for $k = 1$ (planar). We take the gas constant to have the value $\gamma = 7/5 = 1.4$. For $k = 3, 2, 1$, we take $E_{T0} = 0.851072, 0.9781569, 0.538548\,\mathrm{erg}$, so that the shock arrives at $r_{\mathrm{shock}} = 1.0$ at $t = 1\,\mathrm{s}$ for all these three cases.

2.2 RMV heat-conduction benchmark

The RMV problem is defined by [27] and considers a strong point explosion in an ambient gas with nonlinear heat conduction. Self-similar solutions of this problem were discussed by [27]. The reference solution used here is obtained directly from the open-source LANL ExactPack library: `https://github.com/lanl/exactpack`. Details of the reference-solution algorithm are outside the scope of this paper. In this paper, RMV refers to this nonlinear heat-conduction model; the Rosseland-opacity connection and the radiation-hydrodynamics implementation discussed in [29] are mentioned only as historical context.

The energy source of the problem considered here is sufficiently large that heat conduction dominates the fluid flow, and a thermal front leads a hydrodynamic shock. The equations of motion are

$$\begin{array}{l} \frac{\partial \rho}{\partial t} + u\frac{\partial \rho}{\partial r} + \frac{\rho}{r^2}\frac{\partial}{\partial r}(r^2 u) = 0 \\ \frac{\partial u}{\partial t} + u\frac{\partial u}{\partial r} + \frac{1}{\rho}\frac{\partial P}{\partial r} = 0 \\ \frac{\partial e}{\partial t} + u\frac{\partial e}{\partial r} - \frac{P}{\rho^2}\left(\frac{\partial \rho}{\partial t} + u\frac{\partial \rho}{\partial r}\right) = \frac{1}{\rho r^2}\frac{\partial}{\partial r}\left(r^2 \chi \frac{\partial T}{\partial r}\right) \end{array} \qquad (3)$$

where the thermal conductivity is parameterized by

$$\chi(\rho, T) = \chi_0\, \rho^a T^b \qquad (4)$$

where χ_0, a and b are constants, with $a \le 0$ and $b \ge 1$. The conductivity can be related to Rosseland opacity, as discussed by [29]; this relation is retained here only as historical background. The present RMV calculation uses the nonlinear heat-conduction term in (3) and does not solve a radiation-hydrodynamics model. For the problem

under consideration, $a = -2$ and $b = 6.5$. The initial cold-gas density profile is

$$\rho_0(r) = g_0 r^{\kappa} \tag{5}$$

where $\kappa < 0$ and g_0 is a constant. When the exponent κ and the thermal-conductivity exponents a and b satisfy the following relationship, the problem admits a self-similar solution:

$$\kappa = -\frac{6b-1}{2b-2a+1} \tag{6}$$

Thus, $\kappa = -2.111$ in this case. The thermodynamic variables are related by the ideal gas equation of state, $p/\rho = RT = (\gamma-1)e = \Gamma T$. If energy is expressed in units of 10^{16} erg, pressure in units of $10^{16}\,\mathrm{erg\,cm^{-3}}$, temperature in keV, and density in $\mathrm{mg\,cm^{-3}}$, then we set $\Gamma = g_0 = \chi_0 = 1$ in the normalized RMV formulation. These normalized units are used for the RMV calculations below; the dimensional energy corresponding to the initial source is stated separately.

The RMV parameters used in the present calculations are summarized in Table 1.

Table 1 Parameters of the normalized RMV reference problem

Parameter	Value	Definition or unit
γ	5/4	specific-heat ratio
a	-2	density exponent in χ
b	6.5	temperature exponent in χ
κ	-2.111	ambient-density exponent
Γ, g_0, χ_0	1	normalized constants
E_{T0}	235	normalized source energy
t_{ref}	0.5145 ns	comparison time

For the RMV problem [27] considered in the current study, the material is an ideal gas with a specific heat ratio γ of 5/4. The initial total energy is 235.0×10^{16} erg. The reference solution obtained from ExactPack at $t_{\mathrm{ref}} = 0.5145$ ns is used for comparison with the numerical simulations.

The ExactPack output provides the shock position and thermodynamic profiles as functions of time. It is used as the reference solution for this verification study.

3 Numerical models and implementations

3.1 Numerical setup for the classic Sedov problems

In this work, we employ two-dimensional (2D) cylindrical coordinates to simulate point-blast and line-blast problems, and use 2D Cartesian coordinates for the plane-blast problem. The initial conditions consist of a localized high-energy-density region, surrounded by a cold, low-density ambient medium. We set the ambient density to $\rho_0 = 1.0\,\mathrm{g\,cm^{-3}}$, ambient pressure to $p_0 = 0.4 \times 10^{-12}\,\mathrm{dyn\,cm^{-2}}$ (approximating a vacuum), and initial velocity to zero. The ideal equation of state $p = (\gamma-1)\rho e$ is adopted with specific heat ratio $\gamma = 7/5$. The initial energy is deposited in:

- A single center cell for the point-blast case
- A line parallel to the z-axis for the line-blast case
- A line parallel to the x-axis for the plane-blast case

as illustrated in Fig. 1.

For the point-blast and line-blast cases, the computational domain is $[\Delta z/2, 1.2 + \Delta z/2] \times [\Delta r/2, 1.2 + \Delta r/2]$. The origin is located at $[\Delta z/2, \Delta r/2]$, where a small region cut-out has been employed to avoid singularity caused by $1/r$. For the plane-blast case, the computational domain is $[0, 1.2] \times [0, 1.2]$. All cases are performed with uniform grid resolutions of 48×48, 96×96 and 192×192. For the point-blast problem, a 2D axisymmetric grid is employed. The total initial internal energy E_{T0} deposited in the central grid cell is 0.851072. Due to the mirroring of the current symmetric grid along the z-direction, only half of the total deposited energy is considered, i.e. 0.425536. We define e_0 below as the initial specific internal energy; because the ambient density is $\rho_0 = 1$, its numerical value is equal to the corresponding initial energy density divided by ρ_0.

$$e_0^{point-blast} = \frac{E_{T0}/2}{\rho_0 \pi \Delta r^2 \Delta z} \tag{7}$$

For the line-blast problem, a 2D cylindrically symmetric grid is used. The initial internal energy is deposited in the first layer of grid cells along the r-direction. Under the assumption of an infinitely

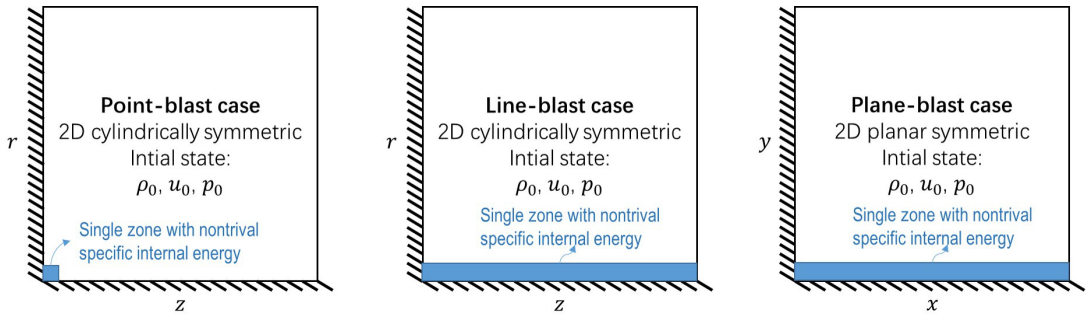

Fig. 1 Initial configurations for the point-, line-, and plane-blast Sedov problems

long line, the total internal energy E_{T0} deposited per unit length of 1 is 0.9781569. The corresponding specific internal energy within the deposition region is:

$$e_0^{line-blast} = \frac{E_{T0}}{\rho_0 \pi \Delta r^2} \tag{8}$$

For the plane-blast problem, a 2D planar symmetric grid is adopted. The initial internal energy is deposited in the first layer of grid cells along the x-direction. Under the assumption of an infinitely large plane, the total internal energy E_{T0} deposited per unit area of 1×1 is 0.538548. The corresponding specific internal energy within the deposition region is:

$$e_0^{plane-blast} = \frac{E_{T0}}{\rho_0 \Delta x} \tag{9}$$

Boundary conditions are set to mirror conditions at the inner boundaries and outflow at the outer boundaries. Note that mirror conditions for the cylindrically symmetric and the planar symmetric are different. For the 2D cylindrically symmetric, the mirror condition is set as $\phi_i = \phi_{i-1}$ for any calculated quantity ϕ_i except velocity ($u_i = -u_{i-1}$), yielding $\phi\left(-\frac{\Delta r}{2}\right) = \phi\left(\frac{\Delta r}{2}\right)$. For the 2D planar symmetric, the mirror condition is set as $\phi_{i+1} = \phi_{i-1}$ for any calculated quantity ϕ_i except velocity ($u_{i+1} = -u_{i-1}$), yielding $\phi(-\Delta x) = \phi(\Delta x)$. The simulation is run until $t_{\text{fin}} = 1.0\,\text{s}$.

3.2 Numerical setup for the RMV benchmark

As in the classic Sedov point-blast test case, the RMV calculation uses two-dimensional rz cylindrical coordinates. The computational domain is $[\Delta z/2, 1.0 + \Delta z/2] \times [\Delta r/2, 1.0 + \Delta r/2]$. The origin is located at $[\Delta z/2, \Delta r/2]$, where a small cut-out avoids the singularity at $r = 0$. Cases are performed with uniform grid resolutions of 40×40, 80×80, and 160×160. In the normalized RMV units defined in Section 2.2, the total energy E_{T0} at the spatial origin is set to 235.0 (equivalent to 235.0×10^{16} erg under the dimensional interpretation). The specific internal energy of the central grid cell depends on the grid size. Taking the 40×40 grid as an example, the grid scale is $\Delta r = 0.025$. Half the volume of the central cell (considering only the $z > 0$ region) is $\pi \Delta r^2 \Delta z = 4.909 \times 10^{-5}$. The density of the central grid cell is $\rho_0 = (\Delta r\sqrt{2}/2)^{-2.111111} \approx 5010.49$, and the specific internal energy of the central grid cell is calculated as:

$$e_0^{RMV} = \frac{E_{T0}/2}{\rho_0 \pi \Delta r^2 \Delta z} \tag{10}$$

The corresponding values for the three grids are listed in Table 2.

Table 2 Grid-dependent central-cell density and specific internal energy for the RMV benchmark

Grid	40×40	80×80	160×160
ρ_0	5010.49009	21646.51170	93518.09108
e_0^{RMV}	477.735757	884.647027	1638.144834

The boundary conditions are consistent with the classic Sedov point blast test case. The calculation terminates at the reference time $t = 0.5145\,\text{ns}$ specified in Section 2.2.

3.3 Numerical implementations

All cases are executed in CFD^2 (Code of Finite Difference for Compressible Fluid Dynamics), developed by Zhang et al. since 2016. This code employs a finite volume method on structured grids and has been utilized to study buoyancy-, shock-, and shear-driven mixing flows across diverse physical conditions [30, 31]. The present paper documents the governing equations, grid configurations, boundary conditions, time-step choices, and reference-solution comparisons needed to reconstruct the test setup and assess the numerical results. The CFD^2 source code is not distributed with this manuscript; the ExactPack reference library is publicly available at the URL given above. The governing equations comprise the mass, momentum, and energy transport equations, expressed as:

$$\frac{\partial \rho}{\partial t} + \frac{\partial \rho u_j}{\partial x_j} = 0 \tag{11}$$

$$\frac{\partial \rho u_i}{\partial t} + \frac{\partial \left(\rho u_i u_j + p\delta_{ij}\right)}{\partial x_j} = 0 \tag{12}$$

$$\frac{\partial \rho E}{\partial t} + \frac{\partial u_j \left(\rho E + p\right)}{\partial x_j} = \frac{\partial}{\partial x_j}\left(\chi \frac{\partial T}{\partial x_j}\right) \tag{13}$$

Here ρ, u, p, E, and T denote density, velocity, pressure, total specific energy ($E = e + u_i u_i/2$), and temperature, respectively. t and x are the temporal and spatial coordinates, respectively, and $i, j = 1, 2, 3$ denote coordinate directions. The left-hand side contains the temporal and convective terms. The right-hand side of the energy equation is the nonlinear heat-conduction term, with χ denoting the thermal-conductivity coefficient. This term is active only in the RMV case and is set to zero in the classic Sedov case. The equation system is closed by the ideal-gas equation of state (EOS) $p/\rho = (\gamma - 1)e$. The hydrodynamic portion of these governing equations (excluding heat conduction) in 2D rz cylindrical coordinates takes the following form:

$$\frac{\partial \rho}{\partial t} + \frac{\partial \rho u_z}{\partial z} + \frac{\partial \rho u_r}{\partial r} = -\frac{\rho u_r}{r} \tag{14}$$

$$\frac{\partial \rho u_z}{\partial t} + \frac{\partial \left(\rho u_z u_z + p\right)}{\partial z} + \frac{\partial \rho u_z u_r}{\partial r} = -\frac{\rho u_z u_r}{r} \tag{15}$$

$$\frac{\partial \rho u_r}{\partial t} + \frac{\partial \rho u_r u_z}{\partial z} + \frac{\partial \left(\rho u_r u_r + p\right)}{\partial r} = -\frac{\rho u_r u_r}{r} \tag{16}$$

$$\frac{\partial \rho E}{\partial t} + \frac{\partial u_z \left(\rho E + p\right)}{\partial z} + \frac{\partial u_r \left(\rho E + p\right)}{\partial r} = -\frac{u_r \left(\rho E + p\right)}{r} \tag{17}$$

Due to the presence of the $1/r$ term, the coordinate in the r-direction must avoid the origin point. Calculations typically start from $\Delta r/2$.

For all computations herein, temporal integration advances via a third-order Runge–Kutta scheme with a CFL number of 0.25. Convection terms are computed using a hybrid WENO5 and HLLC approach. WENO5 refers to the fifth-order weighted essentially non-oscillatory scheme[15]. HLLC denotes the Riemann solver employed to estimate inter-cell numerical fluxes using pressure-based wave speeds[16]. For the RMV problem, the nonlinear heat-conduction term is solved implicitly and coupled to the hydrodynamics solver via operator splitting: the heat-conduction step is followed by a hydrodynamics step.

4 Numerical Results and Discussions

4.1 Classic Sedov results

Simulations of the classic Sedov problems are performed at grid resolutions of 48×48, 96×96 and 192×192 cells. Figure 2 shows density contours for the three Sedov geometries at different resolutions. The wave structures become progressively more similar under grid refinement, and the point-blast density contours retain good angular symmetry.

The results are then compared with the reference solution obtained from ExactPack. Figures 3–5 show density, pressure, and velocity profiles along the y direction for the plane blast, the

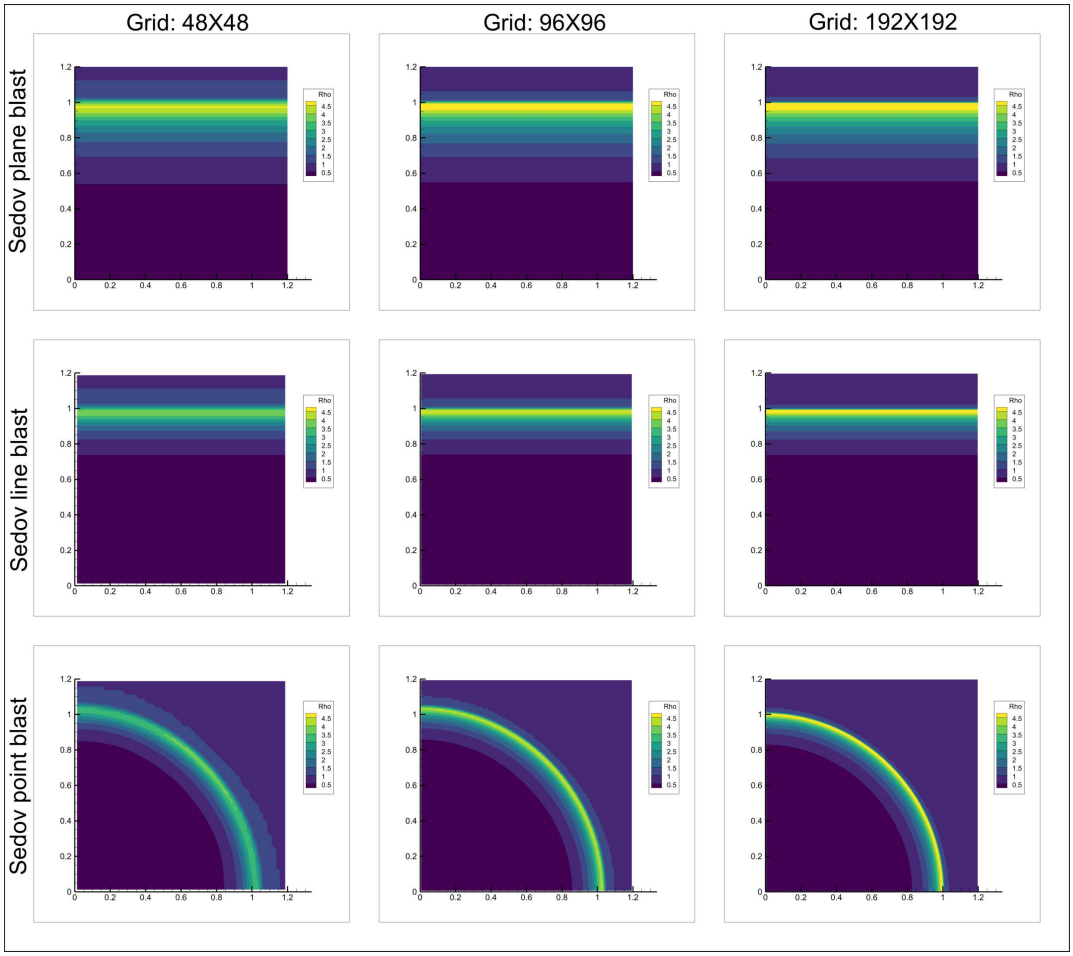

Fig. 2 Density contours for the plane blast (top row), line blast (middle row), and point blast (bottom row) at resolutions of 48×48 (left column), 96×96 (middle column), and 192×192 (right column)

r direction for the line blast, and a direction 45 degrees from the z axis for the point blast. The profiles become more consistent with the reference solution under grid refinement, with the largest discrepancies occurring near the shock front, where numerical diffusion is most pronounced. For the point blast, velocity oscillations remain near the origin after refinement, likely because the deposited energy is concentrated in a single central cell.

4.1.1 Convergence analysis for Sedov problems

This section compares the computed solutions with the reference solution obtained from ExactPack and reports grid-convergence measures. The

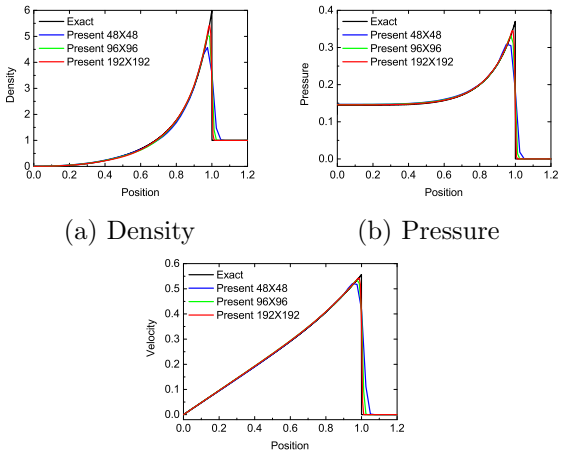

(a) Density (b) Pressure

(c) Velocity

Fig. 3 Density, pressure, and velocity profiles at different grid resolutions for the Sedov plane-blast case

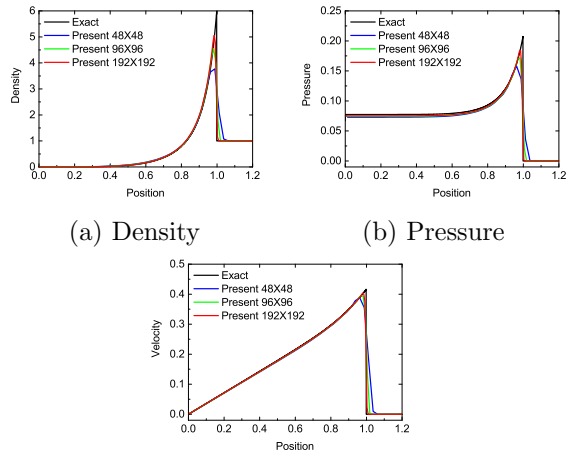

(a) Density (b) Pressure

(c) Velocity

Fig. 4 Density, pressure, and velocity profiles at different grid resolutions for the Sedov line-blast case

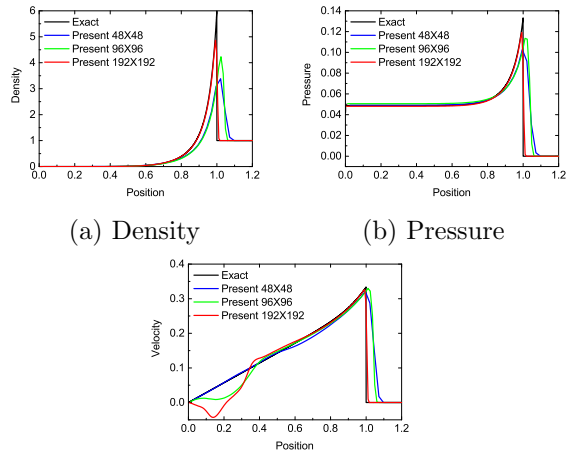

(a) Density (b) Pressure

(c) Velocity

Fig. 5 Density, pressure, and velocity profiles at different grid resolutions for the Sedov point-blast case

convergence rate characterizes how the numerical error changes with grid spacing for the discretized continuum equations[6]. By comparing the error norms between numerical solutions and the reference solution on different grid scales, the convergence order of the numerical solution over the entire domain is quantitatively determined. The definitions of different norms and the corresponding error calculation formulas are as follows:

$$\|e\|_{L^1} = \frac{\sum_{i=1}^{N} |u_i - \tilde{u}_i| \Delta V_i}{\sum_{i=1}^{N} \Delta V_i}$$
$$\|e\|_{L^2} = \sqrt{\frac{\sum_{i=1}^{N} |u_i - \tilde{u}_i|^2 \Delta V_i}{\sum_{i=1}^{N} \Delta V_i}} \quad (18)$$

where u is the numerical solution, $\tilde{u}$ is the reference solution, N is the number of solution points, and ΔV_i is the current element size. The convergence order is computed as follows. For a fine grid with size h_2 (Here, h denotes the linear grid spacing; for the uniform grids used here, $h = \Delta r = \Delta z$.) and numerical solution u_{h_2}, and a coarse grid with size h_1 and numerical solution u_{h_1}, let e_h denote a given norm error between the numerical and reference solutions. The convergence order p is given by:

$$p = \frac{\log\left(e_{h_2}/e_{h_1}\right)}{\log\left(h_2/h_1\right)} = \frac{\log\left(e_{h_2}\right) - \log\left(e_{h_1}\right)}{\log\left(h_2\right) - \log\left(h_1\right)} \quad (19)$$

From the previous profile comparison plots, it can be seen that the velocity profile shows relatively poor agreement with the reference solution. Therefore, this convergence analysis primarily focuses on velocity, as other physical quantities generally exhibit better convergence than velocity. Plots of the logarithm of the L^1 and L^2 norms of the errors in velocity for grid convergence are shown in Figure 6 for the plane blast, line blast and point blast cases. The plots reveal that for both plane and line cases, the L^1 norm of velocity approaches first-order convergence, while the L^2 norm falls below first-order. For the point case, velocity demonstrates the poorest convergence behavior, consistent with the profile comparison results in Figure 5.

4.1.2 Angular reliability of the point-blast solution

To assess the directional reliability of the nominally radial point-blast solution, cross-sections are extracted at 15, 45, and 75 degrees relative to the z-axis on the finest 192×192 grid. Figure 7 shows that the density and pressure profiles, including the wave-front locations, remain largely consistent across these directions. The agreement indicates

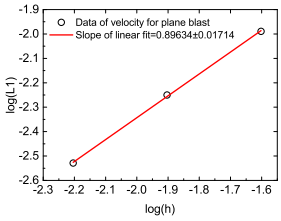

(a) L^1 norm: plane blast

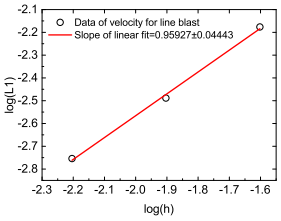

(b) L^1 norm: line blast

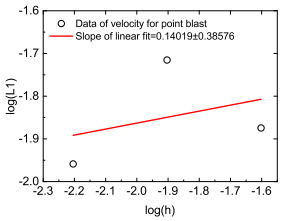

(c) L^1 norm: point blast

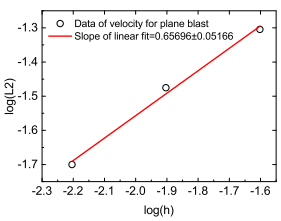

(d) L^2 norm: plane blast

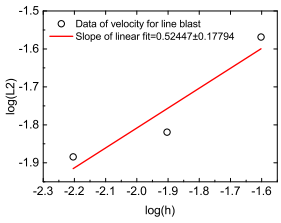

(e) L^2 norm: line blast

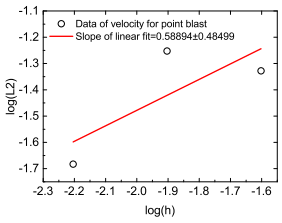

(f) L^2 norm: point blast

Fig. 6 Grid convergence of the L^1 and L^2 velocity-error norms for the Sedov problems

that the resolved shock structure is not strongly dependent on the extraction direction at this resolution and supports the reliability of the reported radial comparisons. This test does not cover velocity: the near-origin velocity oscillations visible in Figure 5 remain a separate central-discretization error and should not be masked by the agreement of density and pressure away from the origin.

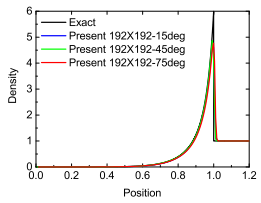

(a) Density

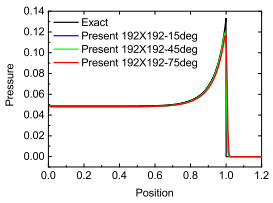

(b) Pressure

Fig. 7 Density and pressure profiles at different extraction angles on the 192×192 grid for the Sedov point-blast case

4.1.3 Reliability with respect to source-region regularization

The point source must be represented by a finite deposition region on the grid, so its size is an independent reliability parameter rather than merely an implementation detail. We first fix the resolution at 192×192 and increase the radius/volume of the initial source region while maintaining constant total energy; consequently, a larger source has a lower initial specific internal energy. Figures 8 and 9 show similar overall wave structures but a systematic outward displacement of the shock as the source region is enlarged. Thus, agreement obtained from a conventional grid study can depend on how the singular source is regularized.

Next, the physical source-region size is held fixed while the grid is refined. Figures 10 and 11 show that the shock-front positions remain largely consistent across the tested grids but stay farther outward than the reference front, whereas the density and pressure peaks are resolved more accurately on finer grids. This separation is important: grid refinement reduces the discretization error in the resolved profiles, but it does not remove the modeling bias introduced by a finite source region of fixed size.

Taken together, these comparisons identify two distinct error controls for a point blast. Reducing the deposition radius improves the representation of the idealized point source and its wave-front location, while increasing the grid resolution improves the resolved peak magnitudes and profile shape. Refinement alone is therefore not a sufficient reliability test when the physical size of the regularized source is retained. The source specification and the mesh spacing must be reported and varied separately when assessing strong point-explosion calculations.

4.2 RMV heat-conduction results

For the RMV heat-conduction problem, the nonlinear conduction term imposes stricter requirements on the time step size. Here we employ a constant time step approach, where finer grids necessitate smaller time step settings. For the 40×40, 80×80, and 160×160 cases, the time steps are set to 2×10^{-4} ns, 5×10^{-5} ns, and 1.25×10^{-5} ns, respectively.

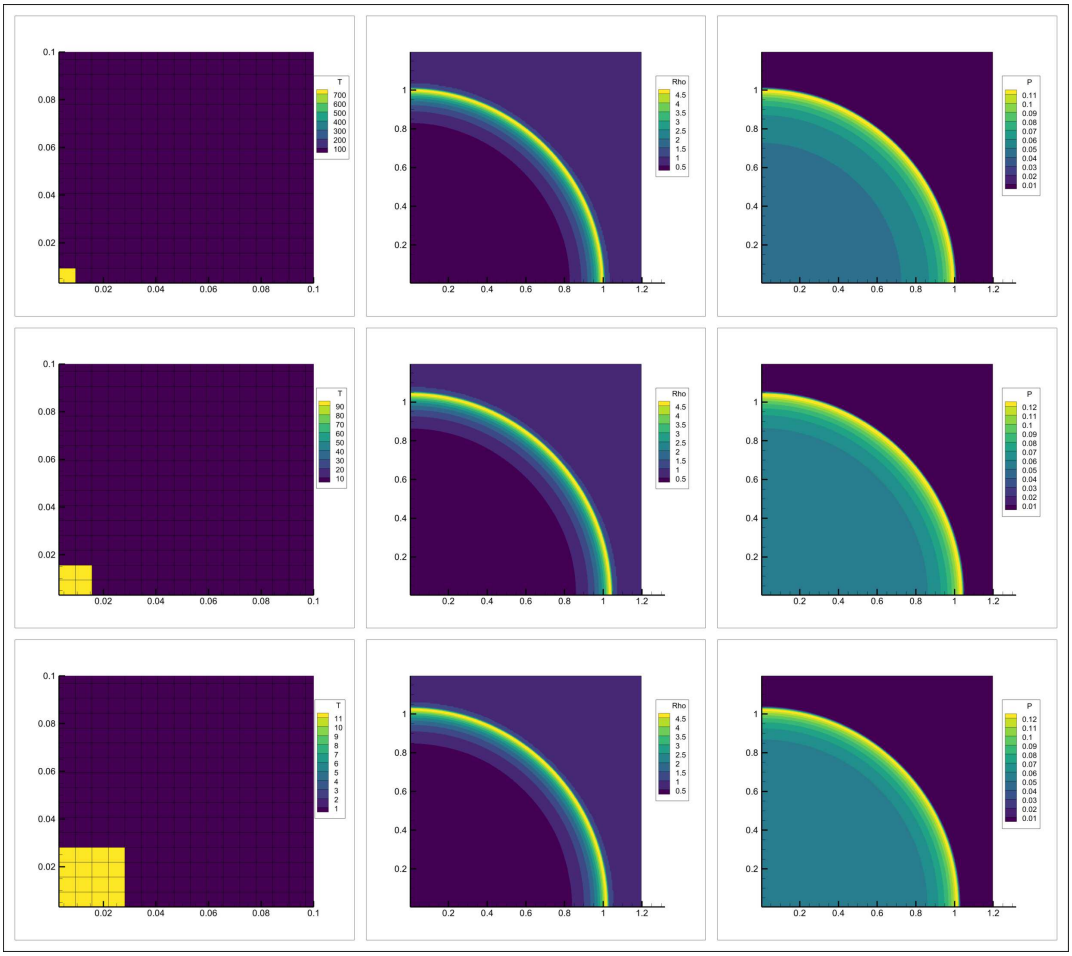

Fig. 8 Effect of initial source-region size in the Sedov point blast on a 192×192 grid: Δr (top row), $2\Delta r$ (middle row), and $4\Delta r$ (bottom row); initial state (left column), final density (middle column), and final pressure (right column)

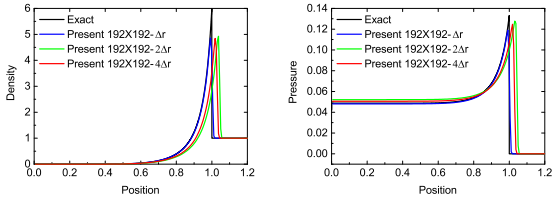

(a) Density (b) Pressure

Fig. 9 Density and pressure profiles for different initial source-region sizes on the 192×192 grid for the Sedov point-blast case

We first present comparisons of density, pressure, and temperature contour plots across different grid resolutions, as shown in Figure 12. The contours show improving visual convergence and symmetry under grid refinement. Temperature exhibits the largest visible changes between the tested resolutions; this observation is consistent with the temperature L^1 and L^2 errors reported below, but no separate sensitivity coefficient is introduced. The initial energy deposition is represented on a discrete grid, and coarser grids can amplify the resulting asymmetry during propagation. In addition, the nonlinear heat-conduction term directly affects the temperature field, while density and pressure are also constrained by the hydrodynamic conservation equations.

The results are then compared with the reference solution obtained from ExactPack. Similar to the Sedov point-blast problem, profiles along the 45-degree direction are extracted for comparison. Figure 13 shows comparisons of density, pressure, radial velocity, and temperature profiles against the reference solution at different grid resolutions. The results exhibit good convergence under grid refinement; the shock locations and

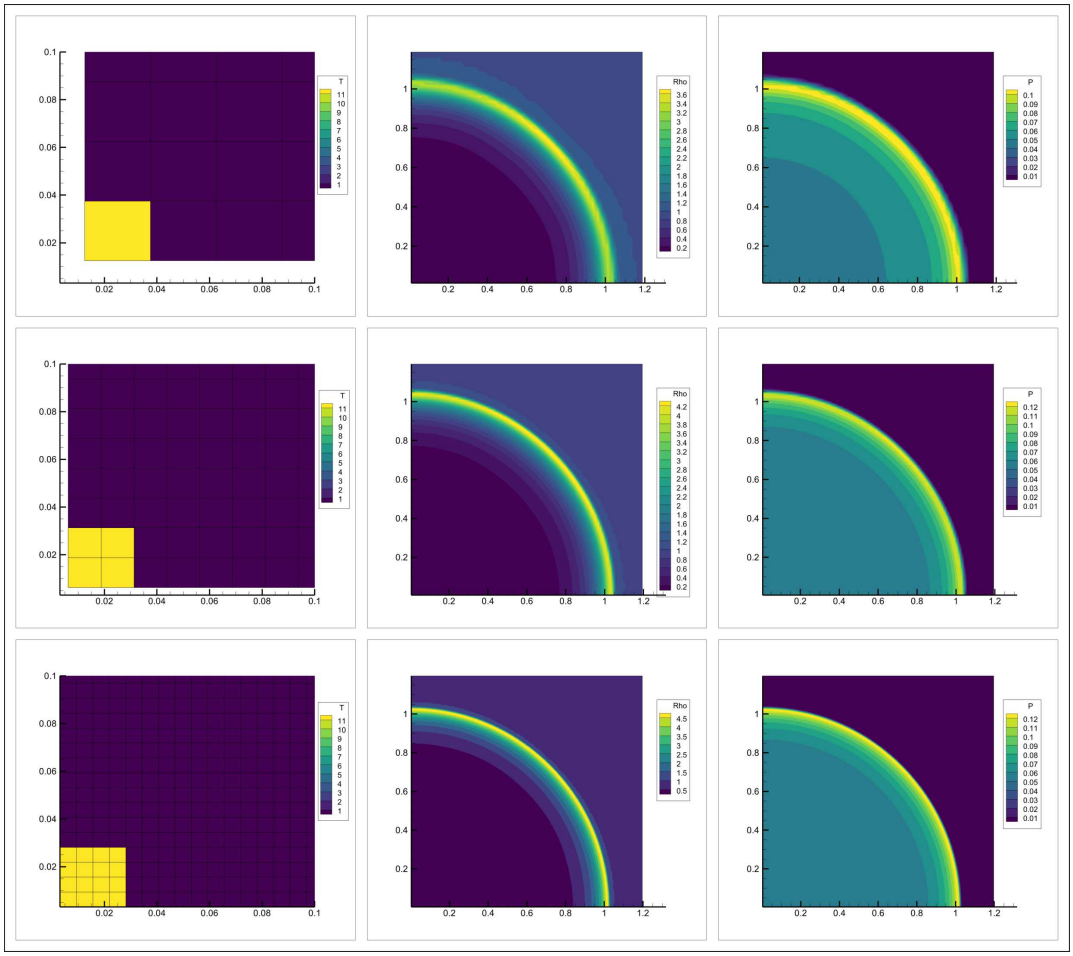

Fig. 10 Sedov point-blast contours at fixed physical source-region size: 48×48 (top row), 96×96 (middle row), and 192×192 (bottom row); initial state (left column), final density (middle column), and final pressure (right column)

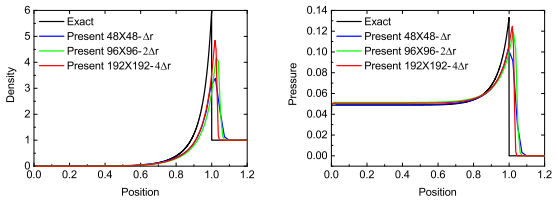

(a) Density (b) Pressure

Fig. 11 Density and pressure profiles at different grid resolutions with a fixed physical source-region size for the Sedov point-blast case

temperature profiles appear consistent with the reference solution in these profile comparisons, although no separate quantitative shock-position error is reported here. Unlike the classic Sedov point-blast case, no significant oscillations appear near the origin in the velocity profiles after grid refinement. The smoother velocity behavior could be related to the regularizing effect of nonlinear heat conduction and the associated broadening of the thermal and hydrodynamic transition regions; the present data do not isolate this mechanism from other discretization effects.

4.2.1 Error analysis and convergence study

Convergence analysis for RMV is presented in this section. Error norms are computed using the same method in Section 4.1.1. The convergence rates for density, velocity, and temperature are shown in Figure 14. For density and velocity, the convergence rates of both L^1 and L^2 norms are ~ 1. Similar convergence rates are observed for the temperature. These rates are close to those reported by [29] for a fully implicit radiation-hydrodynamics

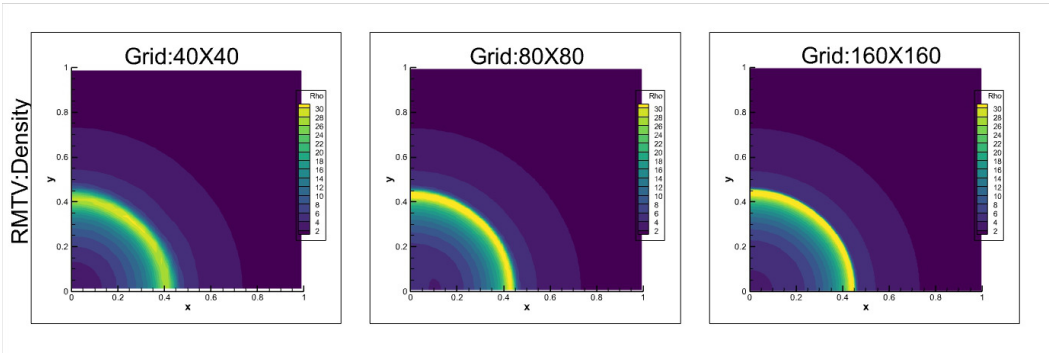

(a) Density

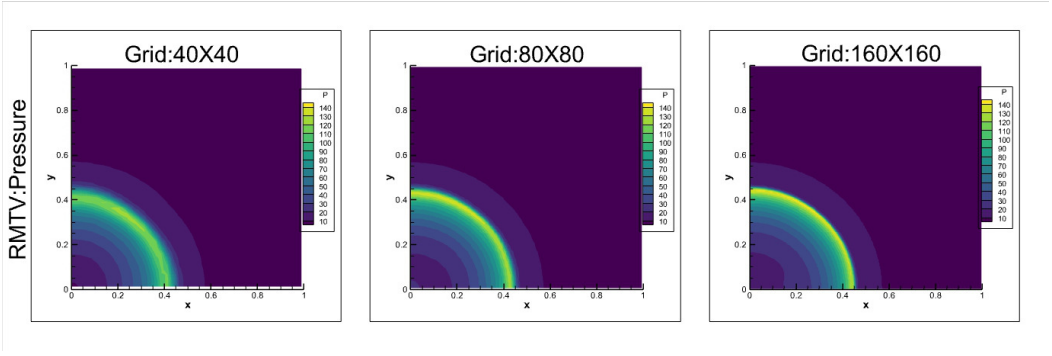

(b) Pressure

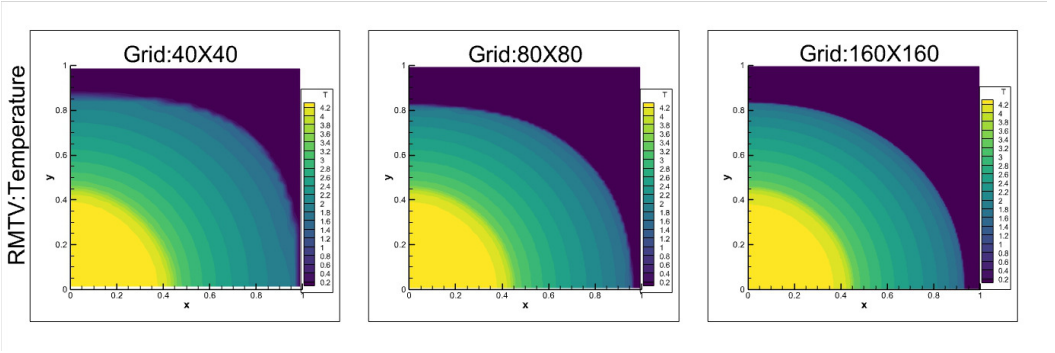

(c) Temperature

Fig. 12 Density, pressure, and temperature contours at different grid resolutions for the RMV case

calculation. This is only a contextual comparison with a related heat-transport calculation, not a validation of the present RMV model against the same physical equations. The RMV results show higher measured convergence rates than the classic Sedov cases in the present tests. This difference is consistent with, but does not establish, a possible smoothing effect of nonlinear heat conduction; an independent controlled comparison would be required to test that interpretation.

4.2.2 Angular reliability of the RMV solution

Directional reliability is further examined on a 320×320 grid. The termination time and source-region settings are consistent with the preceding RMV cases, and the time step is 1×10^{-5} ns because of the smaller grid spacing. Figure 15 compares profiles extracted at 15, 45, and 75 deg relative to the z-axis. The hydrodynamic shock-front positions are largely consistent across the three

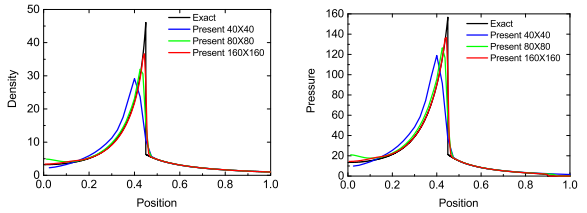

(a) Density (b) Pressure

(c) Velocity (d) Temperature

Fig. 13 Density, pressure, velocity, and temperature profiles at different grid resolutions for the RMV case

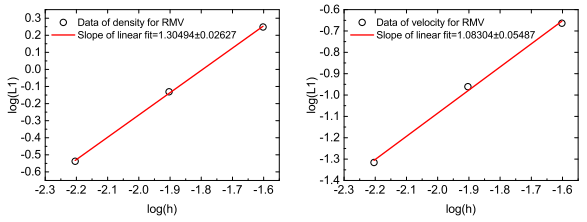

(a) L^1 norm: density (b) L^1 norm: velocity

(c) L^1 norm: temperature (d) L^2 norm: density

(e) L^2 norm: velocity (f) L^2 norm: temperature

Fig. 14 Grid convergence of the L^1 and L^2 error norms for density, velocity, and temperature in the RMV case

directions, while the thermal-wave positions retain a smaller directional variation. This variation is substantially reduced relative to the coarser-grid contours discussed above. The angle test therefore provides a direct reliability check on both waves: hydrodynamic symmetry is already well preserved on the fine grid, and the apparent thermal-wave anisotropy decreases under refinement but is the more sensitive of the two measures.

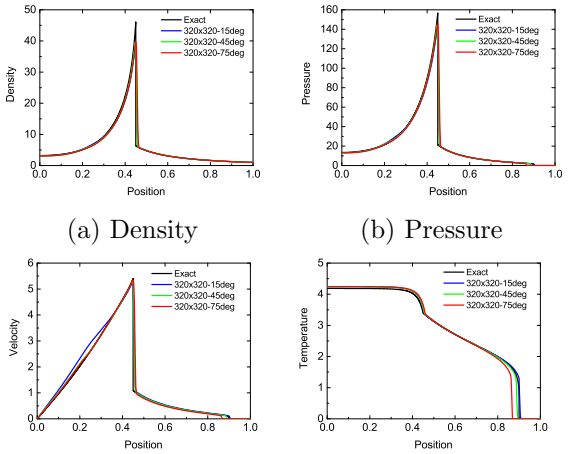

(a) Density (b) Pressure

(c) Velocity (d) Temperature

Fig. 15 Density, pressure, velocity, and temperature profiles at different extraction angles on the 320×320 grid for the RMV case

5 Conclusions

Sedov plane-, line-, and point-blast waves and an RMV point blast with nonlinear heat conduction have been assessed against ExactPack reference solutions. The principal findings are organized below according to the numerical features that determine the reliability of a blast-wave calculation.

First, the computed wave-front locations and profiles approach the reference solutions under refinement for the standard source setup. The source-region experiments nevertheless show that wave-front agreement is not governed by mesh spacing alone. Enlarging the deposition region at fixed resolution moves the Sedov point-blast shock outward. When that enlarged physical source region is held fixed during refinement, the profile peaks improve but the displaced shock front persists. Source regularization therefore introduces a

bias distinct from the ordinary grid-discretization error.

Second, the refined Sedov point-blast density and pressure profiles agree closely at extraction angles of 15, 45, and 75 deg. For the RMV case, the hydrodynamic shock positions are likewise consistent across these directions on the 320×320 grid, while the smaller residual variation of the thermal-wave position identifies temperature transport as the more sensitive symmetry measure. These angular comparisons support the reliability of the radial profile assessment without implying that all variables are equally insensitive to direction.

Third, the measured convergence depends on both geometry and physical coupling. The Sedov plane- and line-blast velocity errors approach first order in the reported L^1 norms, whereas their L^2 rates are below first order and the Sedov point-blast velocity converges least favorably. In contrast, the RMV density, velocity, and temperature errors exhibit approximately first-order measured convergence in both L^1 and L^2 over the tested grids. The comparison shows that convergence measured for a coupled heat-conduction benchmark can differ substantially from that of the corresponding class of discontinuous pure-hydrodynamic blast problems.

Fourth, the largest localized defect in the classical Sedov point blast is the velocity oscillation near the origin. Its persistence under refinement, together with the sensitivity to deposition radius, identifies the discrete representation of the central energy release as a limiting error source. The RMV velocity profiles display weaker near-origin oscillations in the present calculations. This difference is consistent with the broader transitions produced in the heat-conduction-coupled problem, although the present tests do not isolate heat conduction from the other differences between the Sedov and RMV setups and therefore do not establish a causal smoothing mechanism.

Finally, nonlinear heat conduction changes both the observable wave structure and the reliability criteria: the RMV calculation contains distinct thermal and hydrodynamic waves, requires smaller time steps on refined grids, and shows greater directional sensitivity in temperature than in the hydrodynamic variables. The combined results identify central discretization error, finite-source bias, and heat-conduction-coupled convergence as three separate findings that should be checked when assessing multidimensional blast-wave calculations.

The assessment is limited to the present operator-split nonlinear-heat-conduction model. It does not include a separate quantitative global energy-conservation error or a controlled calculation that varies heat conduction while holding all other parameters fixed. More general transport models and fully coupled time integration may therefore exhibit different behavior.

Statements and Declarations

Funding

This work was supported by the National Natural Science Foundation of China (grant nos. 12588301, 12532013 and 12672283) and the National Key Laboratory of Computational Physics (grant no. 6142A05240201).

Competing interests

The authors have no relevant financial or non-financial interests to disclose.

Data availability

The ExactPack reference library used to generate the reference solutions is publicly available at https://github.com/lanl/exactpack. The numerical data underlying the figures are available from the corresponding author on reasonable request.

Code availability

The CFD^2 source code is not publicly available. The open-source ExactPack reference library is available at https://github.com/lanl/exactpack.

References

[1] Sedov, L.I.: Similarity and Dimensional Analysis in Mechanics. Academic Press, New York (1959)

[2] Landau, L.D., Lifshitz, E.M.: Fluid Mechanics, pp. 392–396. Pergamon Press, Elmsford, NY (1959)

[3] Kamm, J.R.: Evaluation of the sedov-von neumann-taylor blast wave solution. Astrophys. J. Suppl. **46** (2000)

[4] Kamm, J.R., Timmes, F.X.: On efficient generation of numerically robust sedov solutions. Technical Report LA-UR-07-2849, Los Alamos National Laboratory, Los Alamos, NM (2007)

[5] Pederson, C., Brown, B., Morgan, N.: The sedov blast wave as a radial piston verification test. Journal of Verification, Validation and Uncertainty Quantification **1**, 031001 (2016)

[6] Kamm, J.R., Rider, W.J., Brock, J.S.: Consistent metrics for code verification. Technical Report LA-UR-02-3794, Los Alamos National Laboratory, Los Alamos, NM (2004)

[7] Chevalier, R.A.: The hydrodynamics of type ii supernovae. Astrophys. J. **207**, 872–887 (1976)

[8] Burrows, A.: Supernova explosions in the universe. Nature **403**(17), 727–733 (2000)

[9] Leonard, T.A., Mayer, F.: Helium blastwave measurements of laser-heated microshell targets. J. Appl. Phys. **46**(8), 3562–3565 (1975)

[10] Petrasso, R.D.: Inertial fusion -rayleigh's challenge endures. Nature **367**, 217–218 (1994)

[11] Thomas, V.A., Kares, R.J.: Drive asymmetry and the origin of turbulence in an icf implosion. Phys. Rev. Lett. **109**(7), 075004–075004 (2012)

[12] Harten, A., Lax, P.D., Leer, B.V.: On upstream differencing and godunov-type schemes for hyperbolic conservation laws. SIAM Review **25**(1), 35–61 (1983)

[13] Harten, A.: High resolution schemes for hyperbolic conservation laws. J. Comput. Phys. **135**(2), 260–278 (1997)

[14] Sweby, P.K.: High resolution schemes using flux limiters for hyperbolic conservation laws. SIAM Journal on Numerical Analysis **21**(5), 995–1011 (1984)

[15] Jiang, G.-S., Shu, C.-W.: Efficient implementation of weighted eno schemes. Journal of Computational Physics **126**(1), 202–228 (1996)

[16] Toro, E.F., Spruce, M., Speares, W.: Restoration of the contact surface in the hll-riemann solver. Shock Waves **4**(1), 25–34 (1994)

[17] Kim, K.H., Kim, C.: Accurate, efficient and monotonic numerical methods for multi-dimensional compressible flows. part i: Spatial discretization. J. Comput. Phys. **208**(2), 527–569 (2005)

[18] Kim, K.H., Kim, C.: Accurate, efficient and monotonic numerical methods for multi-dimensional compressible flows. part ii: Multi-dimensional limiting process. J. Comput. Phys. **208**(2), 570–615 (2005)

[19] Thornber, B., Drikakis, D., Williams, R.J.R., Youngs, D.: On entropy generation and dissipation of kinetic energy in high-resolution shock-capturing schemes. J. Comput. Phys. **227**(10), 4853–4872 (2008)

[20] Thornber, B., Mosedale, A., Drikakis, D., Youngs, D., Williams, R.J.R.: An improved reconstruction method for compressible flows with low mach number features. J. Comput. Phys. **227**(10), 4873–4894 (2008)

[21] Thornber, B., Groom, M., Youngs, D.: A five-equation model for the simulation of miscible and viscous compressible fluids. J. Comput. Phys. **372**, 256–280 (2018)

[22] Zhou, Y.: Rayleigh-taylor and richtmyer-meshkov instability induced flow, turbulence, and mixing. i. Physics Reports **720-722**(C), 1–136 (2017)

[23] Zhou, Y.: Rayleigh-taylor and richtmyer-meshkov instability induced flow, turbulence, and mixing. ii. Physics Reports **723-725**, 1–160 (2017)

[24] Livescu, D.: Numerical simulations of two-fluid turbulent mixing at large density ratios and applications to the rayleigh–taylor instability. Philos. Trans. R. Soc. London A

371(2003), 20120185 (2013)

[25] Dimonte, G., Ramaprabhu, P., Youngs, D., Andrews, M., Rosner, R.: Recent advances in the turbulent rayleigh–taylor instability a. Phys. Plasmas **12**(5), 056301 (2005)

[26] Morgan, B.E., Greenough, J.A.: Large-eddy and unsteady rans simulations of a shock-accelerated heavy gas cylinder. Shock Waves **26**, 355–383 (2016)

[27] Reinicke, P., Meyer-ter-Vehn, J.: The point explosion with heat conduction. Physics of Fluids **A3**(7), 1807–1818 (1991)

[28] Shestakov, A.I.: Time-dependent simulations of point explosions with heat conduction. Physics of Fluids **11**(5), 1091–1095 (1999)

[29] Ghosh, K., Menon, S.V.G.: Fully implicit 1d radiation hydrodynamics: Validation and verification. Journal of Computational Physics **229**, 7488–7502 (2010)

[30] Zhou, Z.-r., Zhang, Y.-s., Tian, B.-l.: Dynamic evolution of rayleigh-taylor bubbles from sinusoidal, w-shaped, and random perturbations. Physical Review E **97**(3), 033108 (2018)

[31] Li, H., He, Z., Zhang, Y., Tian, B.: On the role of rarefaction/compression waves in richtmyer-meshkov instability with reshock. Physics of Fluids **31**(5), 054102 (2019)

[32] Zhang, Y.S., Xie, H.S., Xiao, M.J., He, Z.W., Tian, B.L.: Methodology for determining the coefficients of turbulent mixing model. Journal of Fluid Mechanics **905**(A26), 1–40 (2020)

[33] Xiao, M., Zhang, Y., Tian, B.: Unified prediction of reshocked richtmyer–meshkov mixing with kl model. Physics of Fluids **32**(3), 032107 (2020)

[34] Xiao, M.-J., Zhang, Y.-S., Tian, B.-L.: Modeling of turbulent mixing with an improved K–L model. Physics of Fluids **32**(9), 092104 (2020)

[35] Xiao, M., Zhang, Y., Tian, B.: A k–l model with improved realizability for turbulent mixing. Physics of Fluids **33**(2), 022104 (2021)

[36] Xiao, M.J., Hu, Z.X., Dai, Z.H., Zhang, Y.S.: Experimentally consistent large-eddy simulation of re-shocked richtmyer-meshkov turbulent mixing. Physics of Fluids **34**, 125125 (2022)

[37] Bin, Y., Xiao, M., Shi, Y., Zhang, Y., Chen, S.: A new idea to predict reshocked richtmyer–meshkov mixing: constrained large-eddy simulation. Journal of Fluid Mechanics **918** (2021)

[38] Xiao, M., Qi, H., Zhang, Y.: Local transition indicator and modelling of turbulent mixing based on the mixing state. Journal of Fluid Mechanics **1002**, 4 (2025)